

Effect of SiO₂ on the structure and crystallisation of CaF₂-CaO-Al₂O₃ slag used in electroslag remelting

P.M. Midhun¹ and S. Basu²

1. Graduate student, Indian Institute of Technology Bombay, Powai, Mumbai-400076, INDIA.
Email: 214116001@iitb.ac.in
2. Professor, Indian Institute of Technology Bombay, Powai, Mumbai-400076, INDIA. Email:
somnathbasu@iitb.ac.in

Keywords: slag, flux, silica, structure, ESR, electro-slag

ABSTRACT

Electro-Slag Remelting (ESR) is a process capable of producing ingots with much lower centre-line segregation and better internal soundness than conventional ingot casting processes, as well as lower inclusion and sulphur concentrations. This process is commonly used for alloyed steels intended for critical applications like components of marine turbines, supercritical power plants and rocket motor casings. It involves melting a metal electrode using electrical resistive heating in a slag pool and re-solidification of the resulting metal droplets beneath the slag layer, forming an ingot. Conventional ESR fluxes consist primarily of CaF_2 , Al_2O_3 , and CaO , along with minor concentrations of SiO_2 , MgO , etc.. The emission of fluoride vapour from the molten slag causes several environmental and health problems, triggering a need to develop and reduce the fluoride content in the ESR flux.

The present study aims to develop low- CaF_2 alternatives to commercial ESR fluxes without compromising on productivity and the surface quality of the refined ingot. Thus, the modification in chemical composition needs to satisfy properties like electrical resistivity, viscosity, and liquidus temperature, essential for efficient ESR operation. Since electrical resistivity and viscosity are highly dependent on the ionic structure of the molten slag, it is important to understand the effect of compositional modification on the structure of the flux. The present study employs FT-IR and Raman spectroscopy to investigate the structural variations in the modified fluxes, especially the effect of changing SiO_2 concentration, in comparison with conventional CaF_2 -rich fluxes. Additionally, thermal analysis (DTA/TGA) has been carried out to characterise the melting behaviour of the fluxes. The findings are compared with simulations carried out using the FactSageTM software. Simultaneous analysis of liquidus temperature and the structure is expected to help in identifying the practical suitability of modified ESR flux compositions for industrial implementation.

I. INTRODUCTION

Electro-Slag Remelting (ESR) is one of the processes employed for refining of speciality steels. The metal electrode that needs to be refined is subjected to electrical resistive heating within a slag pool, leading to its melting. Owing to density difference, the molten metal droplets descend through the slag pool, held within a water-cooled copper mould, and re-solidify at the bottom to form an ingot. The slag plays multiple roles during the ESR process. It acts as the heat source through resistive heating, acts as a medium for refining reactions (*e.g.* sulphur removal), dissolves the non-metallic inclusions separating from the molten steel, and controls the surface finish of the solidified ingot by forming a solid slag skin at the ingot-mould wall interface. Figure 1 presents a schematic view of the longitudinal section, showing the key components of the process. Commercially used ESR fluxes typically consist of CaF_2 (30-70%), Al_2O_3 (20-40%) and CaO (20-40%); this range of composition is known to provide an optimal combination of liquidus temperature, viscosity and electrical conductivity in the molten slag. However, CaF_2 -containing slags are prone to evaporation of fluoride vapours during the operation of the ESR, resulting in detrimental effects on the environment as well as the health of the operating personnel (Ju et al, 2022; Zheng, Li and Shi, 2020). Due to this concern, reduction in fluoride concentration in ESR fluxes is being attempted across the globe. However, this endeavour is not easy since the fluoride-containing molten slag offers an optimal combination of liquidus temperature, flow behaviour and electrical properties, thus enabling efficient operation of the ESR process. The key challenge is to identify suitable chemical composition(s) for the molten slag such that its electrical conductivity, viscosity and liquidus temperature would remain within an optimal range, in spite of partial or total replacement of the fluoride content (Wroblewski et al, 2011; Wroblewski et al, 2016).

In addition to the major constituents (Al_2O_3 , CaO and CaF_2), minor quantities of SiO_2 , MgO , etc. are also added to the ESR flux for fine-tuning properties of the molten slag. The presence of SiO_2 in the slag is reported to have a contradicting influence on the ESR process; an increase in SiO_2 concentration tends to improve the surface quality but hinders the overall inclusion content and internal cleanliness of the solidified ingot. Consequently, in most electro-slag remelting practices, the presence of SiO_2 in the flux is considered permissible, but in low concentration (Shi et al, 2015).

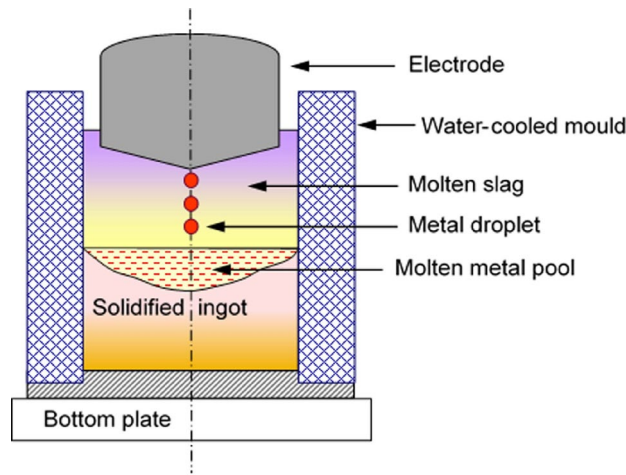


FIG 1 - Schematic view of longitudinal section of the ESR

Numerous studies have been carried out over the past few decades on the influence of varying concentrations of TiO_2 , MgO , etc. on the properties and performance of commercial ESR fluxes (Shi et al, 2017; Ju et al, 2022; Zheng et al, 2020; Zheng, Li and Shi, 2020; Wan et al, 2022; Ju et al, 2022). However, relatively few reports on the modification of ESR flux through SiO_2 addition (Shi et al, 2015; Huang et al, 2021; Xu et al, 2022) are available in the public domain. Information on the structure as well as crystallisation behaviour of these ESR fluxes is also sporadic in literature. In the present study, SiO_2 concentration in a 20% Al_2O_3 -30% CaO -50% CaF_2 commercial ESR flux, commonly employed for refining alloy steels, was modified through small increments, along with a simultaneous reduction in fluoride concentration. Since no studies have been investigated on this commercial flux composition until now, this work will be helpful for researchers and industries involved in ESR. Structural characteristics of the resulting slag were investigated through Raman and FT-IR spectroscopy. The results were crucial for understanding the polymerisation levels in the melt, which would influence the physico-chemical properties such as electrical conductivity and viscosity. The combination of these properties, in turn, would determine the overall suitability of the flux for use in the ESR process. Crystallisation studies were conducted through thermal analysis (DTA/DSC/TGA), which also allowed estimation of the liquidus and solidus temperatures. Thermodynamic simulations were carried out using the “Equilib” module of FactSage™ software; the estimated values were compared with those obtained experimentally.

II. EXPERIMENTAL PROCEDURES

A. Sample preparation

The slag samples were synthesised using laboratory reagent extra pure grade powders of CaF_2 ($\geq 97\%$ Purity), Al_2O_3 ($\geq 99\%$ Purity), CaO ($\geq 90\%$ Purity), and SiO_2 ($\geq 99\%$ Purity) purchased from Loba Chemie Pvt Ltd. As-received Al_2O_3 , CaO and SiO_2 powders were preheated at 1000°C in a muffle furnace to remove adsorbed moisture and decompose any hydroxide/carbonate that might have formed during exposure of the reagents to the ambient atmosphere. Preheating of CaF_2 was carried out at 700°C . A composition of 50% CaF_2 , 20% Al_2O_3 and 30% CaO (by mass) was chosen as the base mix for the flux. Requisite quantities of SiO_2 were added to the base mix, along with a corresponding decrease in CaF_2 content, to generate the entire range of compositions having varying concentrations of CaF_2 and SiO_2 . The thoroughly mixed samples of the approximate total weight of 100g were pre-melted in graphite crucibles (having inner diameter=10cm and depth=10cm) at 1480°C for two hours, followed by rapid quenching in liquid nitrogen. The fluoride content in the slag was measured using the ion-selective electrode (FISE) method, while calcium, aluminum, and silicon concentrations were obtained using Inductively Coupled Plasma Atomic Emission Spectroscopy (ICP-AES: ARCOS from SPECTRO Analytical Instruments, GmbH, Germany). Solution samples for ICP-AES and FISE analysis were prepared through the digestion of the slag samples *via* fusion method. Slag samples are well-mixed with lithium tetraborate and lithium metaborate in a ratio of 1:3:3. The platinum crucibles containing these premixed powders are kept inside a muffle furnace at 1050°C for 30 minutes and consequently dissolved in 1N HCl. In the

measurement of fluorine concentration using FISE method, an electrode has been dipped in the solution to be measured, and the resulting potential difference developed across the membrane has been correlated with the diffusion of fluorine ions from the solution. A few chelating agents (Solutions of Ammonium citrate dibasic, Ammonium tartrate dibasic, Citric acid, Ethylene diamine, EDTA and Sodium chloride) were added to the solution to facilitate the release of fluorine ions from the ionic complexes, ensuring accuracy in measurements (Yeager and Ramanujachary, 2007). Table 1 shows the chemical compositions of the fluxes premelted, and the slag generated. After premelting, the CaF_2 concentration has been decreased, and the CaO concentration has been increased, corresponding to the fluoride evaporation (in forms of SiF_4 , AlF_3 , CaF_2 , HF , etc.) during the chemical reactions at high temperatures (Persson and Seetharaman, 2007). Figure 2 presents the compositional variations within slag sample S2 measured before and after premelting. Even though the $\text{CaO}/\text{Al}_2\text{O}_3$ ratio in the as-mixed powder was initially 1.5, premelting at high temperature caused compositional variations due to the aforementioned reasons, and the ratio was maintained within the range of 1.6-1.7 in every sample.

TABLE 1 - Chemical composition of slag (in mass%)

Slag No	Composition before premelting				Composition after premelting			
	CaF_2	CaO	Al_2O_3	SiO_2	CaF_2	CaO	Al_2O_3	SiO_2
S1	50	30	20	0	44.34	35.46	17.52	0
S2	48.54	29.12	19.41	2.91	37.78	38.13	18.73	2.69
S3	47.16	28.31	18.86	5.66	41.49	32.42	18.22	5.21
S4	45.87	27.52	18.35	8.25	39.82	32.51	16.09	8.92

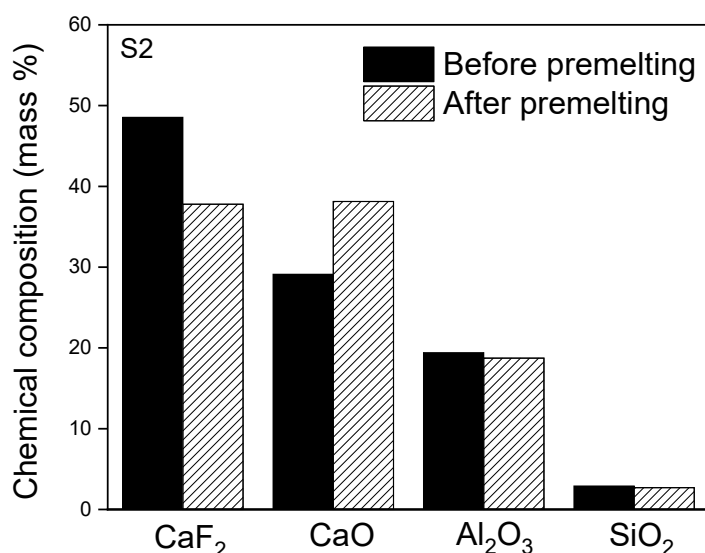


FIG 2 – Chemical composition of slag sample S2 before and after premelting

B. Structural analysis using Raman and FT-IR Spectroscopy

Samples of the quenched slag were analysed using Raman Spectroscopy (Labram HR800 UV from Horiba Jobin Yvon, France) as well as Fourier-Transform Infrared (FT-IR) Spectroscopy (FT/IR-300E from JASCO).

Raman Spectroscopy

The Raman spectra for the slag samples were obtained at room temperature within the wavenumber range of 400 - 2000 cm^{-1} . A laser source with an excitation wavelength of 532 nm was used for all the measurements. The Raman spectra recorded were deconvoluted and fitted using the Fityk software with Gaussian bands.

FT-IR Spectroscopy

IR spectra of the samples were acquired in both absorption and transmission modes, over the wavenumber range of 4000 - 400 cm^{-1} , employing KBr detector. A spectral resolution of 4 cm^{-1} was chosen for all the measurements. The decision to use transmission and absorption modes arose from the fact that different structural aspects (e.g. Si-O-Si bond, O-Al-F bond, etc.) were better revealed under different spectroscopy modes. Each sample was prepared by mixing a particular slag with KBr in a mass ratio of 1:8 in an agate mortar, followed by pressing into pellets. The spectra obtained from the samples, each averaging 50 scans, are subsequently subtracted from the spectrum of "pure" KBr powder in order to obtain the final spectra. The FT-IR absorbance spectra were deconvoluted using the Fityk and Origin software to better reveal the individual peaks, and thus help in understanding the structural aspects. The features better revealed in the transmission spectra did not require any deconvolution.

C. Melting and solidification behaviour

DTA/TGA Analysis

The liquidus temperature of each flux was determined through thermal analysis using a Netzsch™ STA 449 Jupiter unit (from Netzsch Instrument Inc., Germany). The samples were kept in argon atmosphere, with a purge rate maintained at 100 mL/min. For each measurement, close to 30 mg of the pre-melted flux sample was heated at a rate of 20°C/min from room temperature up to 800°C in an alumina crucible. Subsequently, it was further heated at 10°C/min up to 1450°C and held for one minute for homogenisation. Following this, the melt was cooled at a uniform rate of 10°C/min until it reached 800°C after which it cooled to 100°C at the rate of 20°C/min. Typical temperature profile for the experiment is as shown in Figure 3. The Differential Thermal Analysis (DTA) and Thermogravimetric Analysis (TGA) signals of the sample with time and temperature were captured automatically during each cycle and plotted.

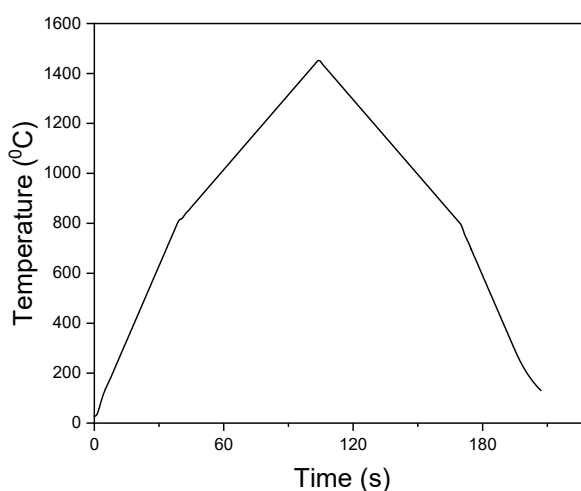


FIG 3 – Temperature profile for DTA/TGA experiment

Thermodynamic simulations

FactSage™ 5.1 software (GTT Technologies, Aachen, Germany) was utilised to simulate the solidus and liquidus temperatures corresponding to the chemical composition of each sample. The Equilib module within FactSage™ was used, together with the FactPS and FToxid databases.

III. RESULTS AND DISCUSSION

A. Analysis of Raman spectra

Figure 4 shows the Raman spectra of the slag samples with varying SiO₂ concentrations. Each sample of molten slag was quenched in liquid nitrogen, with the objective of suppressing phase separations that might otherwise occur during slow solidification. Therefore, the samples were expected to be largely amorphous while retaining any crystalline phase and structural ordering that existed in the melt. In amorphous samples, Raman spectra are often present as envelopes, within which overlapped spectral peaks are responsible for various structural units (Hwa, Hwang and Liu, 1998).

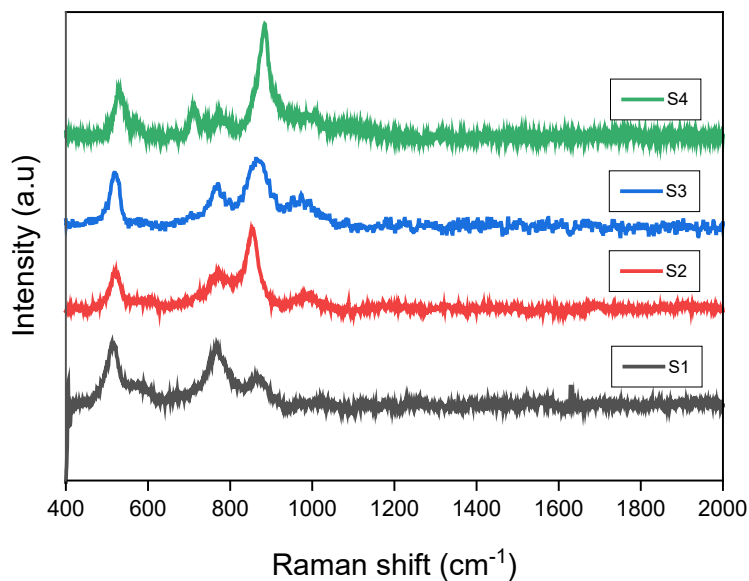


FIG 4 - Raman spectra of samples with various SiO₂ concentrations

In the Raman spectra obtained from the slag samples, similar envelopes were deconvoluted through the Gaussian function to differentiate the individual structural components. The minimum value of the correlation coefficient (R^2) was maintained at 0.96 for this purpose. Fityk software, utilising Gaussian bands, was used for deconvoluting the Raman spectra and fitting the individual peaks. The resulting deconvoluted spectra for all four slag compositions, shown in Figure 5, provide insights into the relative proportions of the structural units and help to illustrate the influence of chemical composition (*viz.* SiO₂ concentration) on the structural feature of each slag.

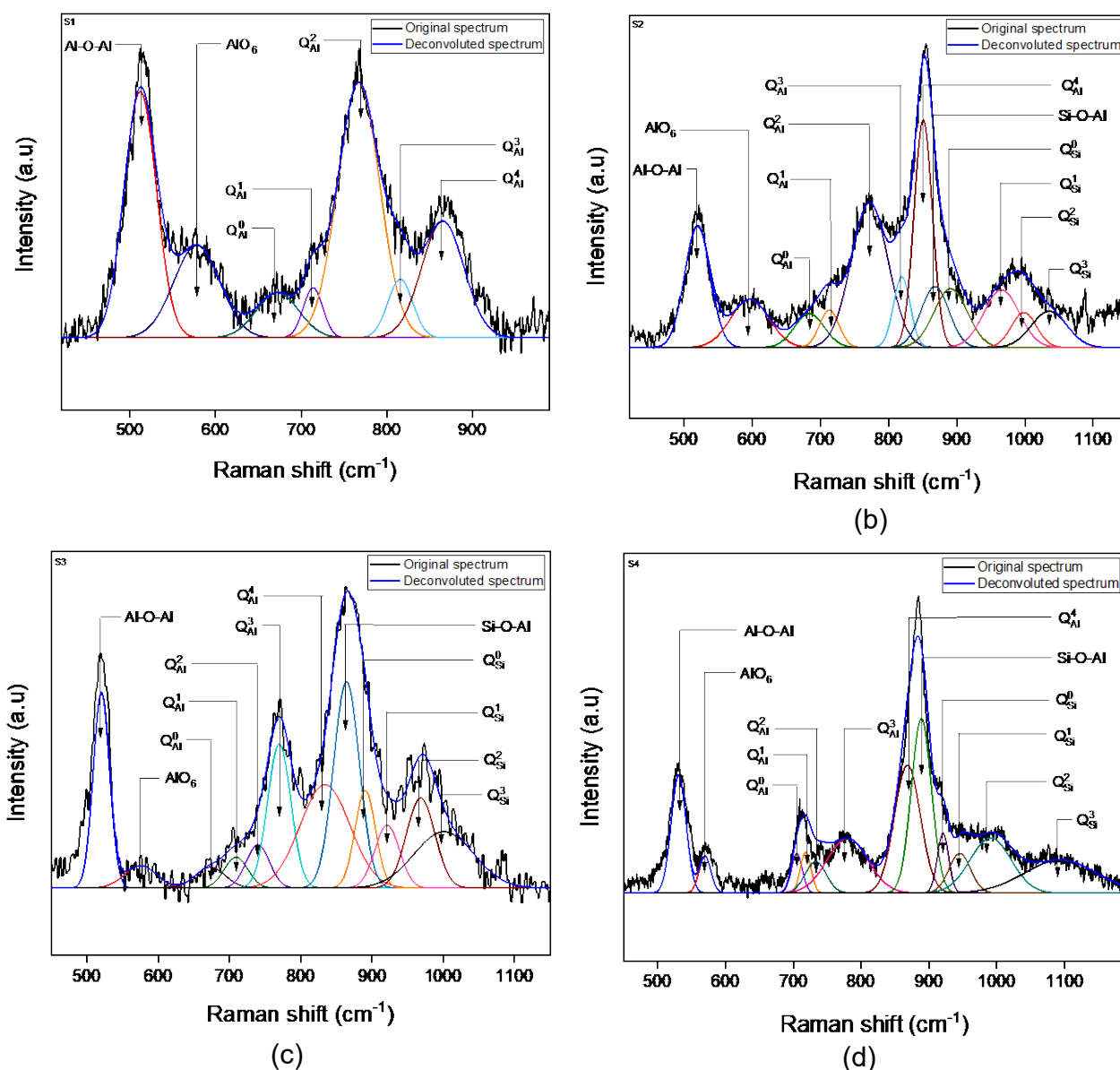


FIG 5 - Deconvolution results of Raman spectra (a)S1 (b)S2 (c)S3 (d)S4

In the silicate network, the absorption peak intensity corresponding to the vibrations of the Si-O covalent bonds in “SiO₄” tetrahedral units varies depending on the population of bridging oxygen in the network. The quantity of bridging oxygens in the “SiO₄” unit is denoted by “n” in “Qⁿ_{Si}”, where n = 0, 1, 2, and 3, correspond to monomer, dimer, chain and sheet structures of silica, respectively. Similarly, “Qⁿ_{Al}” is defined as the “AlO₄” tetrahedral unit with bridging oxygens expressed as “n”, varying over the range 0 - 4. As an example, the Raman shift at ~525 cm⁻¹ in the spectra corresponds to the transverse vibration of bridging oxygen within “Al-O-Al” bonds. Absorption peaks at other Raman shift values similarly represent the vibrations associated with other bonds in the structural units. Table 2 lists the ranges of Raman shift identified in the slag samples bands, and the corresponding structural information (Huang et al, 2021; Zheng et al, 2020; Haghdani, Tangstad and Einarsrud, 2022; McMillan and Piriou, 1983; Li, Shu and Chou, 2014; Hwa, Hwang and Liu, 1998; Kim and Park, 2014).

TABLE 2 - Assignments of raman bands in spectra of CaF₂-Al₂O₃-CaO-SiO₂ slag
(Huang et al, 2021; Zheng et al, 2020; Haghdani, Tangstad and Einarsrud, 2022)

Raman shift (cm ⁻¹)	Raman Assignment and type of vibrations
500-552	Transverse motion of bridging oxygen in Al-O-Al linkages
578-609	AlO ₆ stretching vibrations
665-695	Q ⁰ _{Al} - symmetric stretching vibration of Al-O bonds in AlO ₄ tetrahedra (zero bridging oxygen)
700-738	Q ¹ _{Al} - symmetric stretching vibration of Al-O bonds in AlO ₄ tetrahedra (one bridging oxygen)
748-765	Q ² _{Al} - symmetric stretching vibration of Al-O bonds in AlO ₄ tetrahedra (two bridging oxygen)
788-805	Q ³ _{Al} - symmetric stretching vibration of Al-O bonds in AlO ₄ tetrahedra (three bridging oxygen)
820-855	Q ⁴ _{Al} - symmetric stretching vibration of Al-O bonds in AlO ₄ tetrahedra (four bridging oxygen)
859-880	Si-O-Al stretching vibrations
890-910	Q ⁰ _{Si} - symmetric stretching vibration of Si-O bonds in SiO ₄ tetrahedra (zero bridging oxygen)
915-940	Q ¹ _{Si} - symmetric stretching vibration of Si-O bonds in SiO ₄ tetrahedra (one bridging oxygen)
940-990	Q ² _{Si} - symmetric stretching vibration of Si-O bonds in SiO ₄ tetrahedra (two bridging oxygen)
1000-1070	Q ³ _{Si} - symmetric stretching vibration of Si-O bonds in SiO ₄ tetrahedra (three bridging oxygen)

The integrated area under the curve for each deconvoluted peak may be considered as proportional to the fraction of the corresponding structural unit in the slag sample. Variations in these fractions with respect to the change in SiO₂ concentration in the slag samples are shown in Figure 6. From this figure, it is evident that a rise in SiO₂ concentrations in the slag leads to an enhancement in the intensity of the spectral peak associated with “Si-O-Al” vibrations. This can be correlated with the more intense vibration of “Si-O-” bonds with higher SiO₂ content. This vibration is conducive to the “AlO₄” tetrahedral structures forming complex “Si-O-Al” bonds in the slag structure. Consequently, there is a rise in complex networks and polymerisation in the slag increases. In the context of alumina-tetrahedral units, an increase in Q³_{Al} and Q⁴_{Al} networks was observed, along with a corresponding decrease in Q⁰_{Al}, Q¹_{Al}, and Q²_{Al} networks, as shown in Figure 6. These observations suggest a noticeable increase in the polymerisation of alumina tetrahedra upon the addition of SiO₂ (up to 9 mass%) to the selected flux composition. In silicate networks, the simple networks Q⁰_{Si} and Q¹_{Si} exhibit a decrease, while the proportions of complex Q²_{Si} and Q³_{Si} increase upon the addition of

SiO₂. Thus, it can be inferred that the degree of polymerisation of both silicate and alumina networks was enhanced upon increasing SiO₂ concentration.

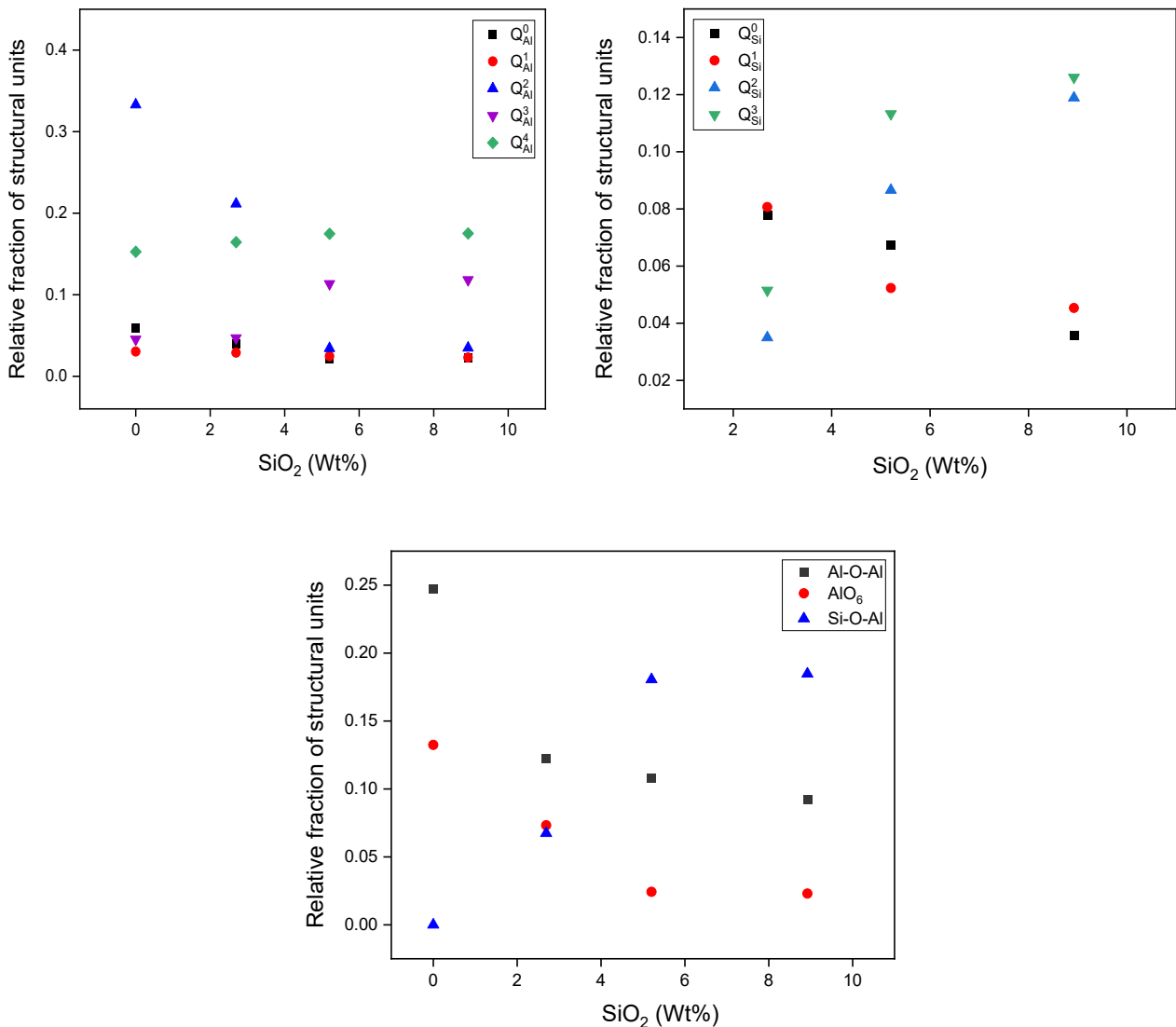


FIG 6 - Relative fraction of structural units in CaF₂-Al₂O₃-CaO-SiO₂ slag from Raman spectra with various SiO₂ concentrations

B. Structural analysis of slag using FT-IR spectroscopy

Both the transmittance and absorbance spectra from the slag samples were obtained using FT-IR spectroscopy. Analysis of transmission depths corresponding to various structures present within the slag in the transmittance spectra provided information about changes in the polymerisation behaviour within each slag sample after SiO₂ addition, especially visible variations on the spectra associated with SiO₄ and AlO_nF_{4-n} structures. As well as, the deconvolution of curves from the absorbance spectra of each sample could provide quantitative information about the presence of distinct structural units inside AlO₄ and SiO₄ structures and gave better clarity about variation in absorption associated with AlO_nF_{4-n} structures, which was difficult to differentiate from some smaller structural units of SiO₄ from the analysis of transmission spectra due to overlapping. Combining both of these sets of information provides a more detailed understanding about the variation in the polymerisation behaviour of slag samples after silica addition.

Figure 7 presents the Fourier Transform Infrared (FT-IR) transmittance spectra of the quenched slag samples. By comparison with prior investigations, the different ranges of wave number associated with specific structural units of interest have been identified and are listed in Table 3. For example, the transmission characteristics over the wave number range of 1200-800 cm⁻¹ represents the asymmetric stretching of “Si-O” bonds within “SiO₄” tetrahedral units, while that over the 800-600

cm^{-1} range is associated with the asymmetric stretching of “Al-O” bonds in “ AlO_4 ” tetrahedral units (Park, Min and Song, 2002; Hwa, Hwang and Liu, 1998; Ju et al, 2022). Owing to the chemical composition, the slag samples investigated are likely to contain “ SiO_4 ” and “ AlO_4 ” tetrahedral units with varying bridging oxygen, represented by the parameters “ Q^n_{Si} ” for silicate units and “ Q^n_{Al} ” for aluminate units (“ n ” = 0 - 4). A similar situation has been indicated in the previous section (on Raman spectra) as well.

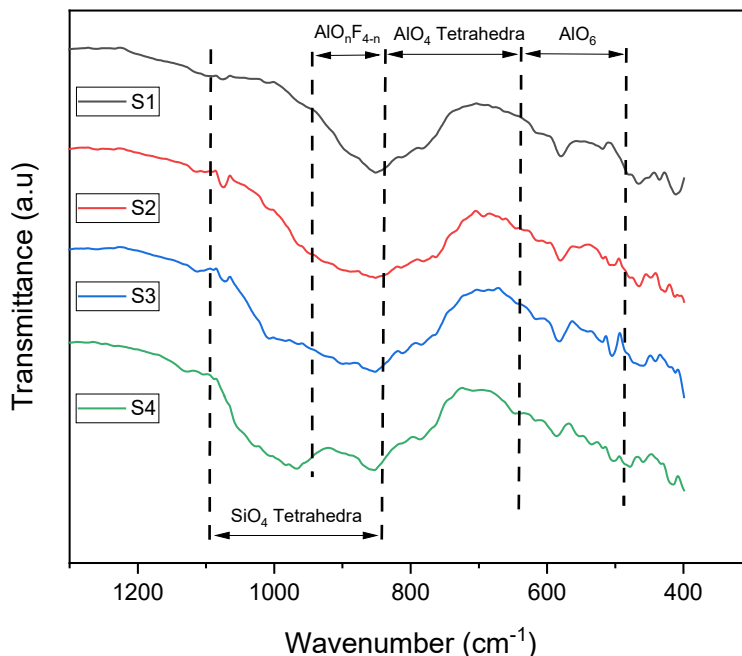


FIG 7 - The FT-IR spectra (transmittance) of the liquid nitrogen quenched $\text{CaF}_2\text{-Al}_2\text{O}_3\text{-CaO-SiO}_2$ flux samples with various SiO_2 contents

It can be seen in Figure 7 that the transmission peak corresponding to “ $\text{AlO}_n\text{F}_{4-n}$ ” in sample S1 (0 mass% SiO_2) is stronger than in the SiO_2 -containing samples over the wave number range $820\text{-}940\text{ cm}^{-1}$. This may be attributed to the possibility of simpler silicate units (Q^0_{Si} and Q^1_{Si}) contributing to the transmission signal over the same wavenumber range in samples S2, S3 and S4, in addition to the contribution from “ $\text{AlO}_n\text{F}_{4-n}$ ” structural units. Based on this, it can be inferred that sample S1 contains a higher fraction of “ $\text{AlO}_n\text{F}_{4-n}$ ” units in comparison with the other slag samples. Upon careful observation around 1050 cm^{-1} , the transmission peak broadens and increases in intensity with increasing SiO_2 concentration, indicating vibrations associated with more complex Q^2_{Si} and Q^3_{Si} structural units. However, it was difficult to distinguish between the overlapping peaks associated with “ AlO_4 ” and “ AlO_6 ” structural units in the transmittance spectrum, for each of the slag samples. Therefore, FT-IR spectra of all the samples were acquired in the absorption mode as well. The resulting absorbance spectra were deconvoluted to identify the contributions from the individual structural units.

Figure 8 illustrates the deconvoluted FT-IR absorption spectra of all four slag samples, which were fitted using Gaussian functions with the Fityk software. Table 3 lists the FT-IR wave number ranges associated with the individual structural units that were identified after deconvoluting the absorbance spectra (Park, Kim and Sohn, 2011; Kim and Sohn, 2013; Lao et al, 2019; Ju et al, 2021).

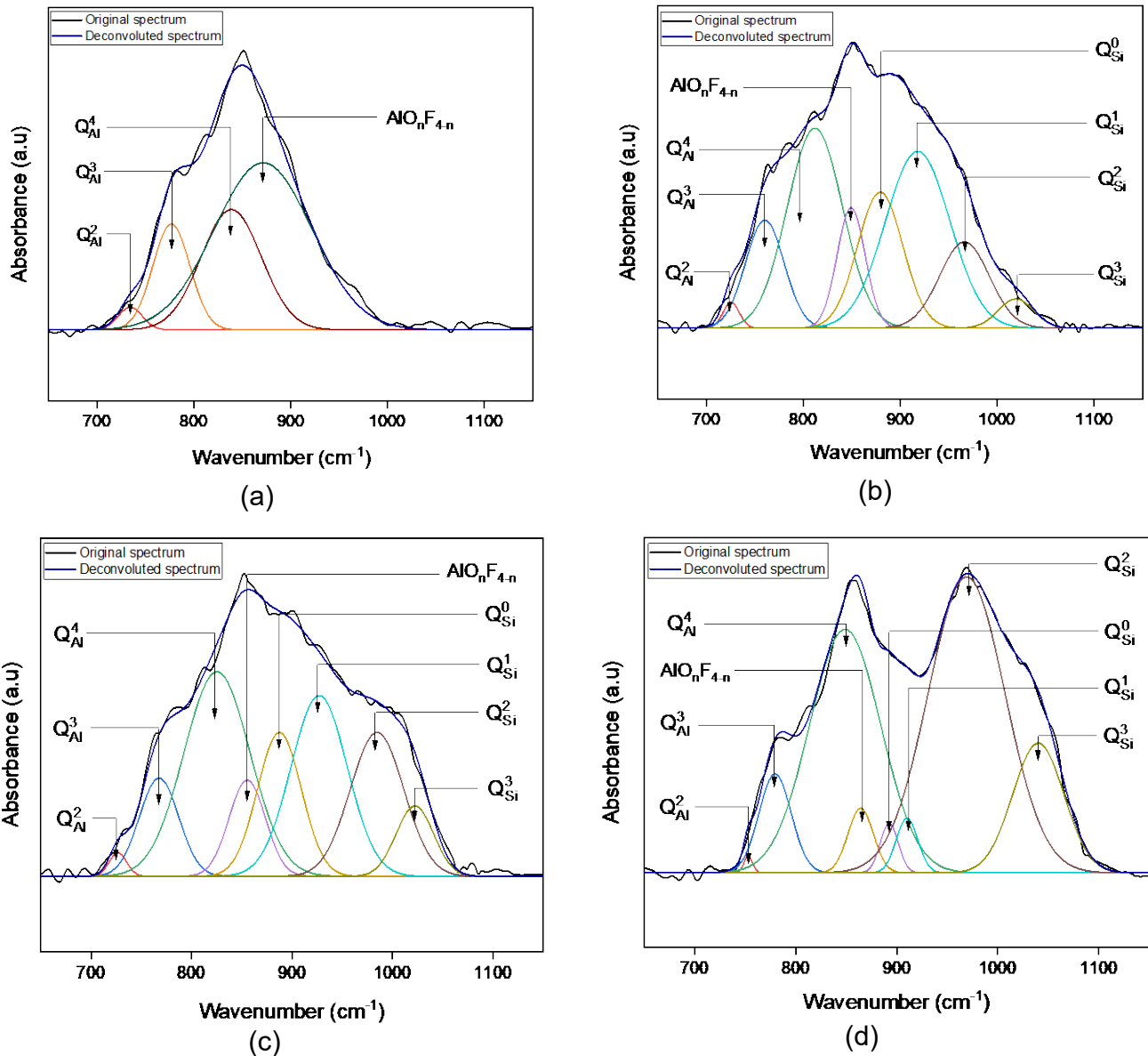


FIG 8 - The deconvolution results of FT-IR absorbance spectra (a) S1 (b) S2 (c) S3 (d) S4

In Figure 9, “relative fraction of structural units” in each sample has been calculated from the deconvoluted peaks of absorption spectra and plotted against the increase in SiO₂ concentration in the slag samples. It has been observed from the plot that the addition of SiO₂ into the selected base flux composition results in a continuous decrease in the presence of “AIO_nF_{4-n}” networks. This can be attributed to the relative reduction in the fraction of fluorine and alumina in the system following the addition of SiO₂. From the analysis of the variation of different structural units within the silicate tetrahedral networks, it is observed that complex structural units, i.e., Q³_{Si} and Q²_{Si}, show an increase, while smaller structural units like Q⁰_{Si} and Q¹_{Si} decrease. This trend signifies an increase in the polymerisation within silicate network structure. Upon further analysis of the graphs, it is observed that simple alumina tetrahedral units, Q²_{Al} and Q³_{Al}, decrease with the addition of SiO₂, while the complex network, Q⁴_{Al} increases. These observations align with the inferences obtained from Raman spectroscopy, which also indicate behaviour of increase in the polymerisation of silicate and aluminate networks upon the addition of SiO₂ into the system.

Before introducing silica (SiO₂) into the “50%CaF₂-20%Al₂O₃-30%CaO” flux system, the system predominantly contained alumina tetrahedral networks with calcium cations serve for charge balance. However, with the addition of SiO₂, silica forms tetrahedral network structures, and basic oxides/fluorides such as CaF₂ and CaO attempt to break these network structures, resulting in the formation of various simple/complex structural units of silica. In the presence of silica networks,

aluminium in alumina units will try to enter silicate networks to form “Si-O-Al” bonds, giving rise to the development of complex networks like Q^3_{Al} and Q^4_{Al} . In the case of silica tetrahedral networks, it is observed that the introduction of SiO_2 into the flux results in an increase in complex tetrahedral units (Q^2_{Si} and Q^3_{Si}), accompanied by a decrease in simple units, such as Q^0_{Si} and Q^1_{Si} . Because the basic oxides/fluorides available in the melt structure are almost constant, and when more silica is introduced into the melt, available oxides/fluorides will try to break down more complex networks initially.

The results obtained from FT-IR spectroscopy and Raman spectroscopy show an increase in the level of polymerisation within both silica and Alumina tetrahedral networks due to the addition of SiO_2 into the selected base composition. These structural variations could influence the physicochemical properties such as viscosity and electrical conductivity of the slag. As the polymerisation level within the melt increased gradually upon adding SiO_2 , viscosity and electrical resistivity values are expected to rise. However, further experiments are recommended to validate these inferences.

TABLE 3 - Assignments of FT-IR bands in spectra of $CaF_2-Al_2O_3-CaO-SiO_2$ slag
(Park, Kim and Sohn, 2011; Lao et al, 2019; Ju et al, 2021)

Wavenumber Range (cm ⁻¹)	Types of vibrations in FT-IR
850-890	Q^0_{Si} - asymmetric stretching vibration of Si-O bonds in SiO_4 tetrahedra (zero bridging oxygen)
910-930	Q^1_{Si} - asymmetric stretching vibration of Si-O bonds in SiO_4 tetrahedra (one bridging oxygen)
960-990	Q^2_{Si} - asymmetric stretching vibration of Si-O bonds in SiO_4 tetrahedra (two bridging oxygen)
1030-1070	Q^3_{Si} - asymmetric stretching vibration of Si-O bonds in SiO_4 tetrahedra (three bridging oxygen)
800-940	Asymmetric stretching vibrations of AlO_nF_{4-n}
490-600	Asymmetric stretching vibration of Al-O bonds in AlO_6 octahedra
610-630	Q^0_{Al} - asymmetric stretching vibration of Al-O bonds in AlO_4 tetrahedra (zero bridging oxygen)
650-670	Q^1_{Al} - asymmetric stretching vibration of Al-O bonds in AlO_4 tetrahedra (one bridging oxygen)
690-720	Q^2_{Al} - asymmetric stretching vibration of Al-O bonds in AlO_4 tetrahedra (two bridging oxygen)
730-760	Q^3_{Al} - asymmetric stretching vibration of Al-O bonds in AlO_4 tetrahedra (three bridging oxygen)
770-820	Q^4_{Al} - asymmetric stretching vibration of Al-O bonds in AlO_4 tetrahedra (four bridging oxygen)

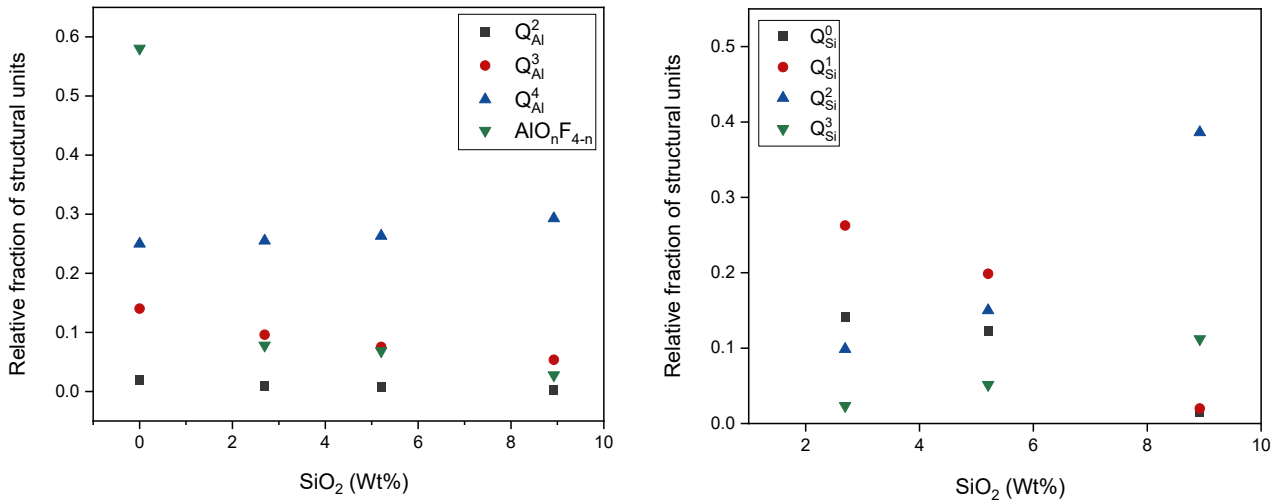


FIG 9 - Relative fraction of structural units in CaF₂-Al₂O₃-CaO-SiO₂ slag from FT-IR absorbance spectra with various SiO₂ contents

C. Analysis of melting and solidification behaviour

Analysis of FactSage™ simulations

The Equilib module of FactSage™ software has been used to collect preliminary information on solidus-liquidus temperatures of the selected slag compositions, which can help identify the expected temperature range where the major phase transitions occur for the selected compositions.

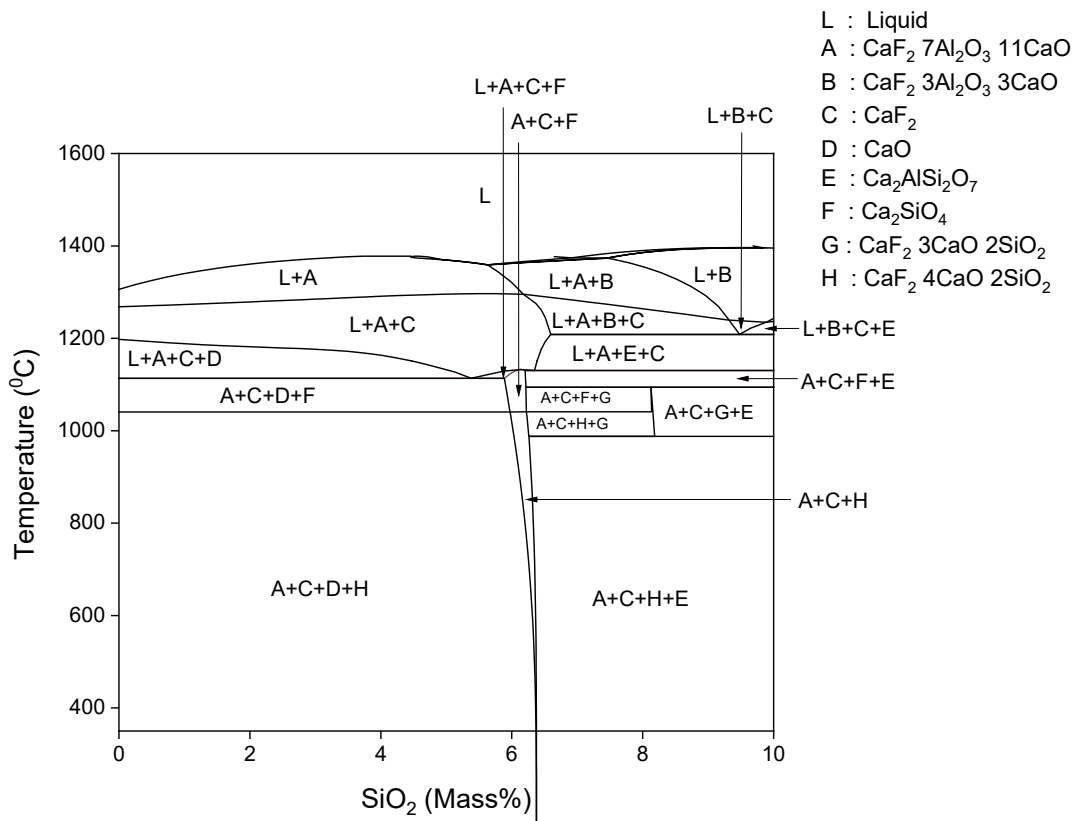


FIG 10 – The phase diagram plotted through FactSage™ simulation (X-axis indicates the concentration of SiO₂ added into 50%CaF₂-20%Al₂O₃-30%CaO)

Figure 10 shows the phase diagram plotted using FactSage™ simulation, where the X-axis shows the addition of SiO₂ concentration in mass% in a slag system containing 50%CaF₂-20%Al₂O₃-30%CaO. Furthermore, from the Equilib module in the FactSage™, information on the formation of various product phases and their fractions under equilibrium conditions at different temperatures can be collected as output data, and this information has been used to plot the graphs showing the variation of the fraction of phases formed during the solidification of the slag samples, as shown in Figure 11. From these figures, liquidus and solidus temperatures for all four slag samples have been estimated. Liquidus temperature represents the temperature at which solidification initiates from 100% liquid, and solidus temperature represents the temperature at which the whole liquid disappears on cooling.

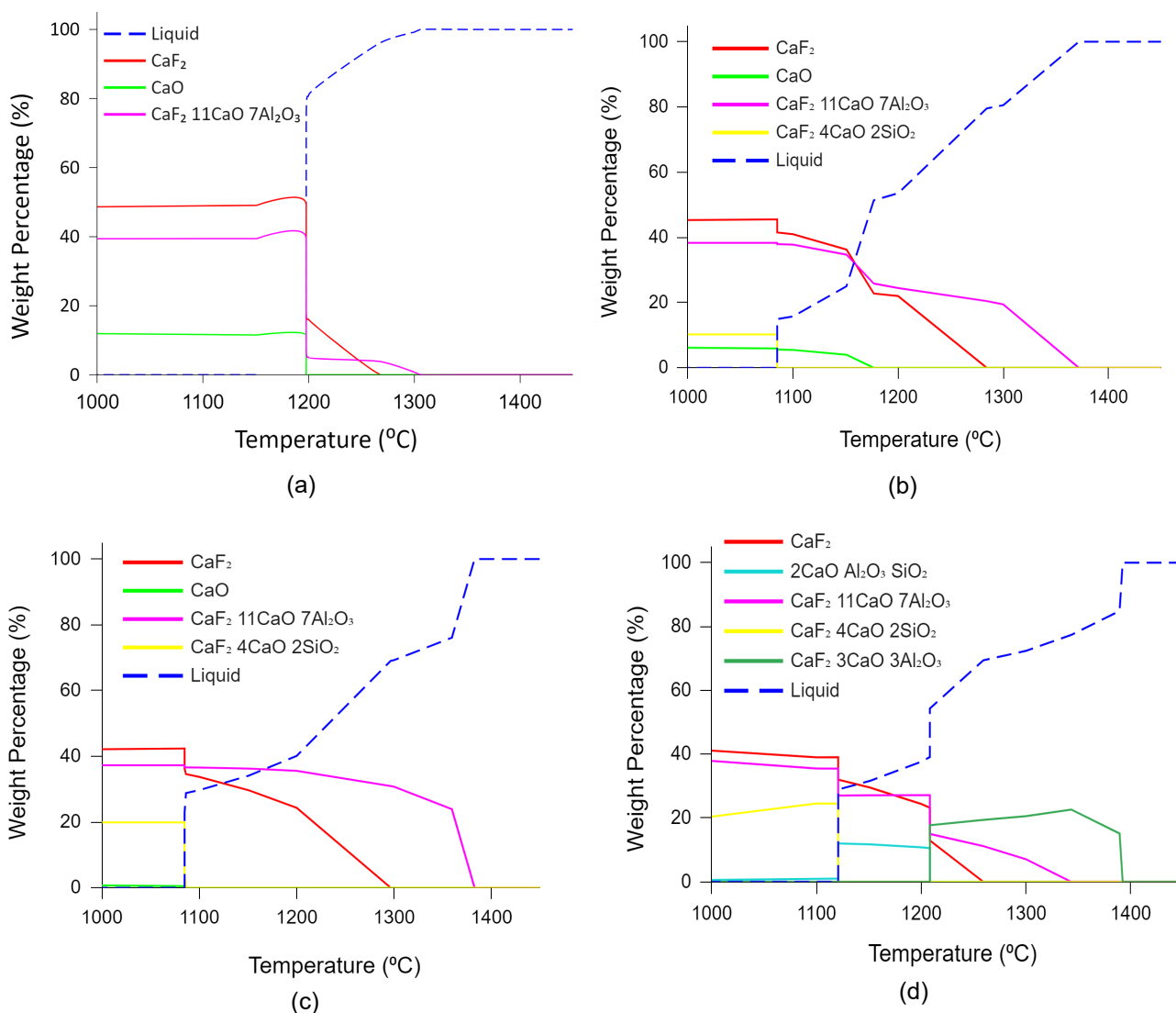


FIG 11 - Crystallisation behaviour of the fluxes calculated using FactSage™ (a)S1 (b)S2 (c)S3 (d) S4

DTA/TGA analysis

Figure 12 shows the DTA and TGA curves of all four slag samples. The liquidus temperature of a slag is defined as the temperature at which the liquid phase initiates transformation to the solid phase during the cooling cycle or the temperature at which the solid sample is fully transitioned into liquid in the heating cycle. The solidus temperature is the temperature at which the first liquid phase forms in a heating cycle or the temperature at which the whole liquid phase transforms to the solid phase in the cooling cycle. Uniform heating and cooling rates of 10⁰C/min are performed for all fluxes in the temperature range of 800°C to 1450°C to determine and compare the liquidus and solidus temperatures. In the plots, the downward peaks are considered to be endothermic peaks. For

example, from the DTA plots, the endothermic peaks observed during the heating cycle are analysed to estimate the liquidus temperature of the slag samples.

In Figure 12, the sudden variations from the DTA curve while changing the heating/cooling rate, represented by the symbol "#", can be associated with the thermal hysteresis. In the present work, these variations are not considered exo/endothermic peaks during the analysis. The symbols "•" and "x" in the curve denote estimated liquidus and solidus temperature, respectively. Further, the significant peaks observed between the temperature range of 800-1450°C in both heating and cooling cycles for all four slag samples are presented in Figures 13 and 14 respectively.

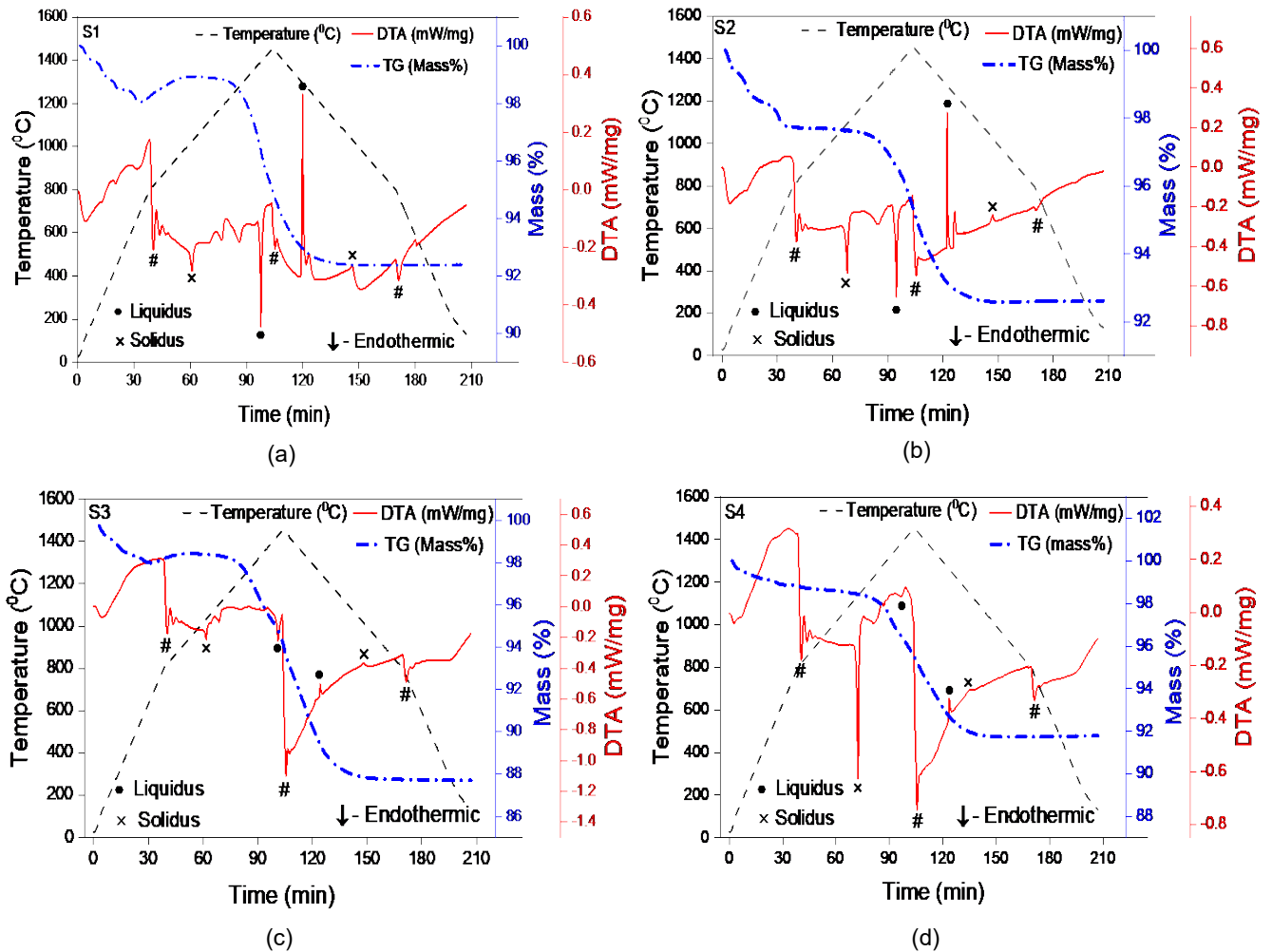
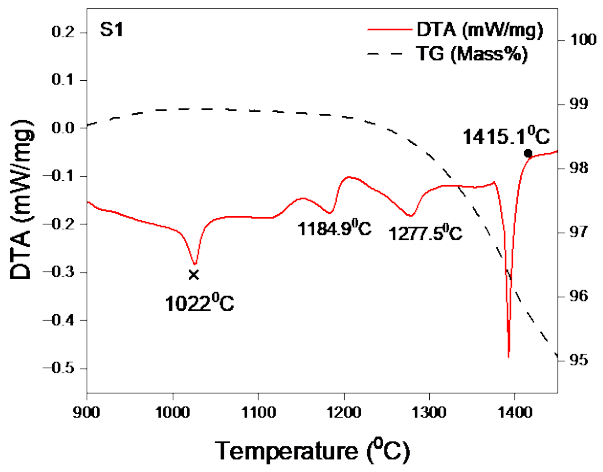
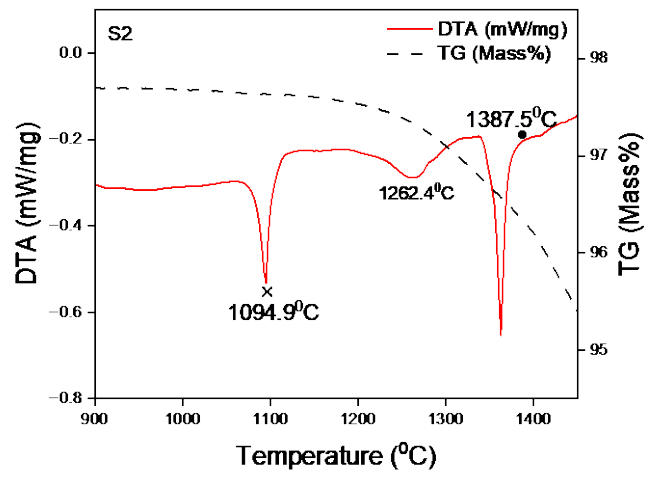


FIG 12 - DTA/TGA curves of the $\text{CaF}_2\text{-Al}_2\text{O}_3\text{-CaO-SiO}_2$ slag melts (a) S1 (b) S2 (c) S3 (d) S4

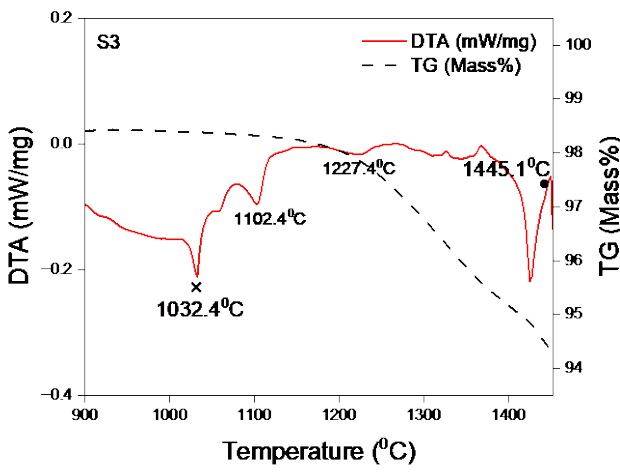
In the heating cycle, following the energy required to overcome the nucleation barrier, the start of the formation of the liquid phase can be considered as the peak point of the first endothermic peak. Further, following the intermediate phase transformations during melting, the last endothermic peak observed in the cycle indicates the completion of solid-to-liquid phase transformation. The liquidus temperature is estimated from the point at which the curve regains its linearity following the final peak, showing that the slag sample is expected to be fully transitioned to the liquid phase. During the cooling cycle, crystallisation begins at the temperature associated with the first observed peak. After overcoming the energy required for the nucleation barrier, the temperature at which the first crystalline phase formed is considered as the peak point of the initial peak in the cooling cycle, representing the liquidus temperature. Following this, multiple peaks can be observed, corresponding to the possibility of crystallisation temperature of various intermediate phases formed, eventually leading to the last peak associated with the formation of the final phase and the complete solidification of slag. The solidus temperature in the cooling cycle is interpreted as the temperature at which the DTA curve regains its linearity following the final observed peak. Figures 13 and 14 present the estimation of liquidus and solidus temperature according to this convention.



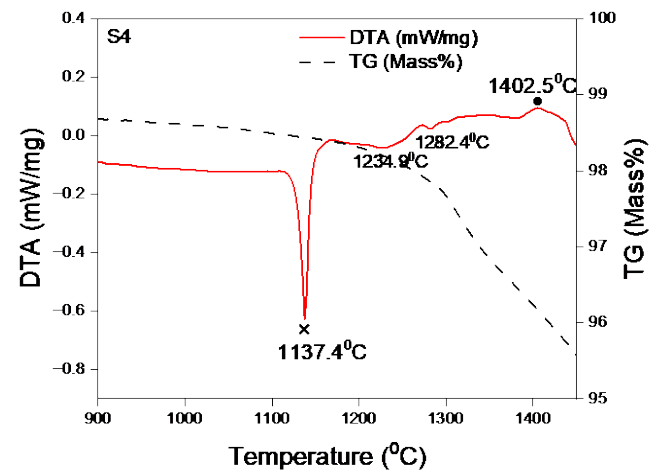
(a)



(b)



(c)



(d)

FIG 13 - DTA/TGA curves of the $\text{CaF}_2\text{-Al}_2\text{O}_3\text{-CaO-SiO}_2$ slag melts in heating cycle
 (a) S1 (b) S2 (c) S3 (d) S4

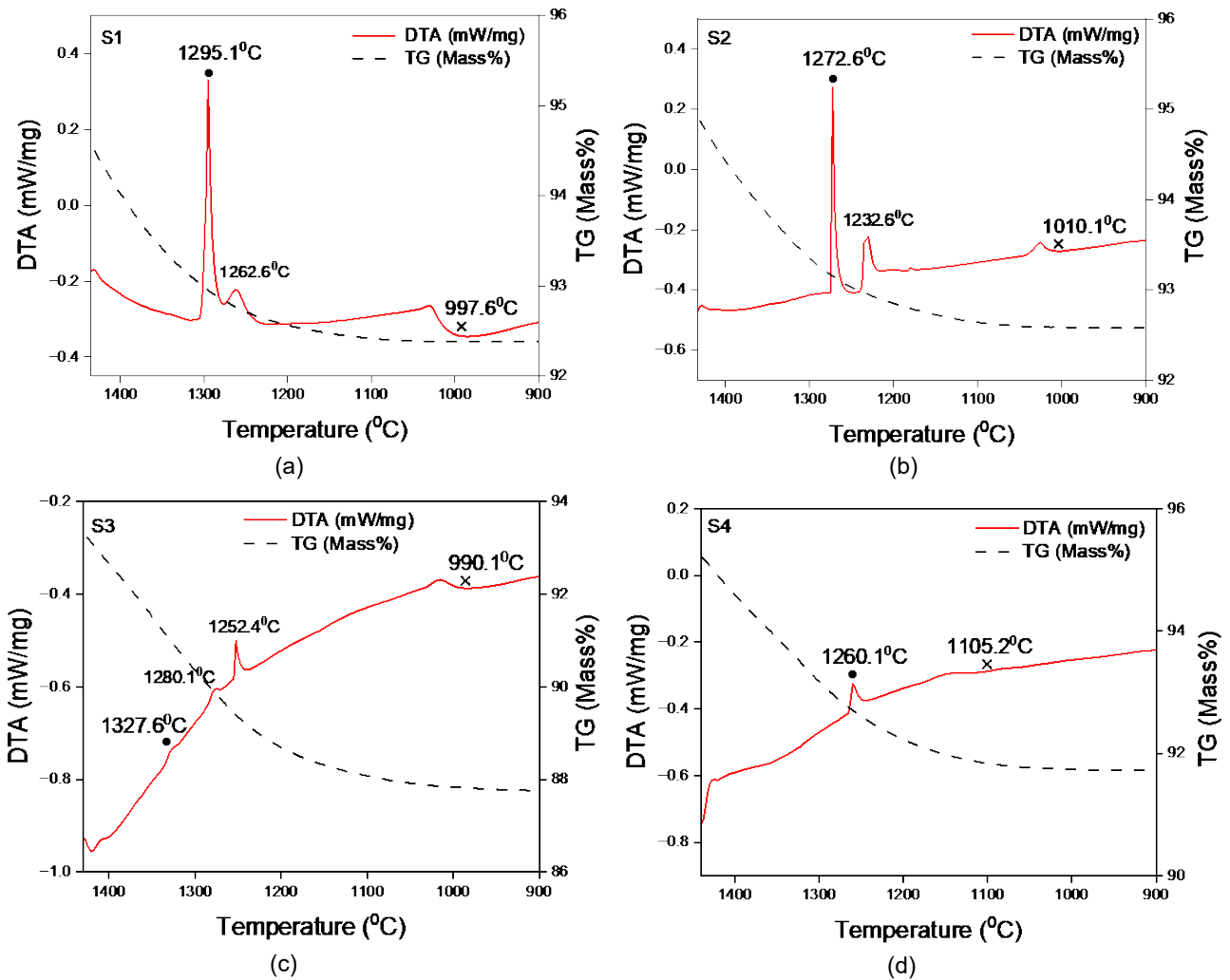


FIG 14 - DTA/TGA curves of the $\text{CaF}_2\text{-Al}_2\text{O}_3\text{-CaO-SiO}_2$ slag melts in cooling cycle
 (a) S1 (b) S2 (c) S3 (d) S4

After analysing the DTA curves, it is evident that the studied slag samples exhibit a high degree of undercooling in the cooling cycle, leading to the delayed observation of crystallisation peaks. Figure 15 shows the variation in the presence of exothermic peak associated with liquidus temperature in the cooling cycle due to undercooling from the slag sample S1. In the present work, considering these aspects of undercooling along with the knowledge of the mass loss due to fluoride evaporation at high temperature at the end of the heating cycle causing compositional changes, the selection of solidus-liquidus temperature values is determined from endothermic peaks from the heating cycle.

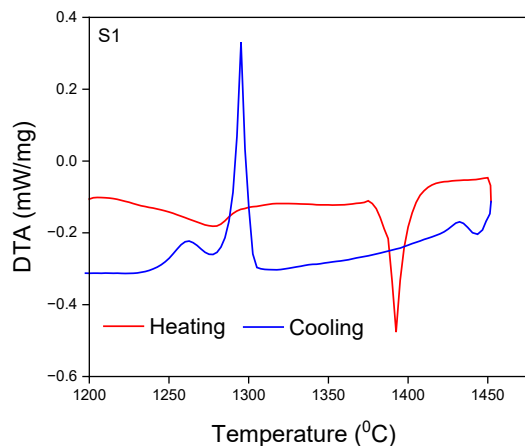


FIG 15 – DTA curve of slag sample S1 showing a high degree of undercooling

Table 4 presents solidus and liquidus temperature information of all the slag samples determined from Figure 13, i.e., during the heating cycle. The peaks observed between the solidus and liquidus temperatures in DTA results can be due to the possible potential phase transformations within this temperature range, as reported by some previous works with similar slag samples (Huang et al, 2021). The plotted graphs from FactSage™ data shown in Figure 11 can further support this inference, as they show certain thermodynamically possible intermediate phase transitions between solidus and liquidus temperatures. For validating the presence of phases in the slag samples, the XRD characterisation has been performed on all four samples, quenched from 1000°C. Results are presented in Figure 16. The major phases identified in the analysis are ‘CaF₂ 11CaO 7Al₂O₃’ and ‘CaF₂’. The results closely match with those of FactSage™ simulation as presented in Figure 11, where, in all the slag samples, major phases present below solidus temperature are these identified phases from XRD. However, further studies are recommended to confirm this and identify the reason for the formation of the aforementioned phases and the formation of peaks. TGA results indicate a mass drop of approximately ~10% for all the slag samples following holding at 1450°C, which can possibly be due to the fluoride evaporation from the samples (Ju et al, 2023; Ju et al, 2021). Table 4 represents a comparison of the predicted solidus-liquidus temperatures from FactSage™ and results obtained from DTA analysis.

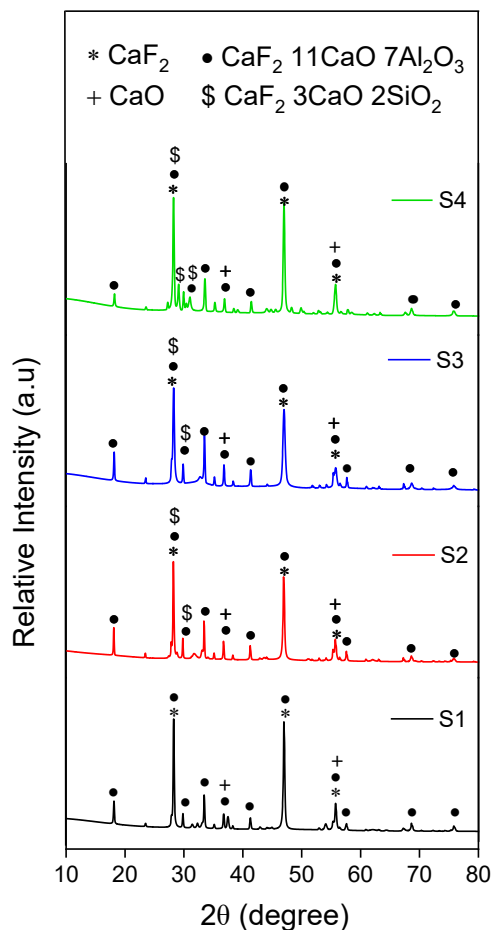


FIG 16 – XRD analysis of slag samples quenched from 1000°C

After the addition of SiO₂ into the ESR slag selected for the study, which is used for refining special alloy steels, the liquidus temperatures of the fluxes undergo changes with respect to compositional and structural modifications. However, for refining commonly used special alloy steels, the measured values of liquidus and solidus temperatures are within acceptable range, as the liquidus temperatures of the fluxes are below those of commonly used alloy steel grades. Furthermore, it is suggested to conduct the ESR refining using the modified fluxes and analyse the efficiency of the ESR process as well as the quality of refined ingots for a better understanding of the suitability of these fluxes.

TABLE 4 - Estimation of solidus and liquidus temperatures from DTA and FactSage™

Slag No	Solidus (°C)		Liquidus(°C)	
	FactSage™	DTA	FactSage™	DTA
S1	1197.7	1022	1305.9	1415.1
S2	1084.9	1094.9	1371.8	1387.5
S3	1084.9	1032.4	1382.5	1445.1
S4	1120.7	1137.4	1392.2	1402.5

IV. CONCLUSIONS

In this study, the influence of SiO₂ concentration on the structural characteristics and melting-solidification behaviour of the “CaF₂-Al₂O₃-CaO-(SiO₂)” slag was systematically investigated. Structural analyses conducted through Raman spectroscopy and FT-IR spectroscopy techniques revealed significant changes in the polymerisation behaviour of alumina and silica units with varying SiO₂ concentrations. Changes in the relative fraction of structural units have been analysed through Raman and FT-IR spectroscopy techniques, indicating increased level of polymerisation in both alumina and silicate networks. The estimation of liquidus and solidus temperatures, performed using FactSage™ software and DTA/TGA analysis, further supported the suitability of the flux in ESR operation. The conclusions are summarised as follows.

(1) In raman spectroscopy results, within alumina-tetrahedral units, an increase in Q³_{Al} and Q⁴_{Al} networks was observed, with a corresponding decrease in Q⁰_{Al}, Q¹_{Al}, and Q²_{Al} networks, suggesting an increase in alumina tetrahedra polymerisation with SiO₂ addition into the selected commercial flux composition. Silicate networks show a decrease in simple networks (Q⁰_{Si} and Q¹_{Si}) and an increase in complex networks (Q²_{Si} and Q³_{Si}) after the addition of SiO₂, indicating an increase in the polymerisation of silicate tetrahedral networks.

(2) In FT-IR analyses, within silicate tetrahedral networks, an increase in complex structural units (Q³_{Si} and Q²_{Si}) and a decrease in smaller structural units (Q⁰_{Si} and Q¹_{Si}) were observed, indicating increased polymerisation level of the silicate network. Within alumina networks, a decrease in simple alumina tetrahedral units (Q²_{Al} and Q³_{Al}) and an increase in the complex network Q⁴_{Al} were observed, and results suggest that the addition of SiO₂ increases the polymerisation of alumina tetrahedral networks, consistent with the results from Raman spectroscopy.

(3) After the addition of SiO₂ in the slag, silica forms tetrahedral networks, and basic oxides/fluorides (CaF₂ and CaO) try to break these networks, creating various simple and complex structures in silica. Aluminium from alumina units will try to join silicate networks, forming ‘Si-O-Al’ bonds and leading to complex networks like Q³_{Al} and Q⁴_{Al}. In silica tetrahedral networks, the gradual addition of SiO₂ increases complex units (Q²_{Si} and Q³_{Si}) and reduces simpler ones like Q⁰_{Si} and Q¹_{Si}. The reason for the rise in complex structural units can be that, after the addition of more silica, the basic oxides/fluorides in the melt, which is at a constant level across all compositions, initially break relatively more complex networks.

(4) Liquidus temperature measurements obtained from FactSage™ and DTA/TGA analyses show that the fluxes’ liquidus temperatures are within permissible ranges, i.e., they were found to be below the melting point of the ingot to be refined, ensuring the suitability of the flux for the refining of various alloy steel grades.

ACKNOWLEDGEMENTS

The authors are thankful for the support received from the Science and Engineering Research Board (SERB), India, towards fellowship for one of the authors as well as the conduct of the experiments. We express our sincere gratitude to our colleagues in the Ferrous Process Laboratory and Geochemistry lab at IIT Bombay for their invaluable support in conducting this work.

REFERENCES

- Haghdani, S, Tangstad, M and Einarsrud, K E, 2022. A Raman-structure model for the viscosity of SiO₂-CaO-Al₂O₃ system, *Metallurgical and Materials Transactions B*, 53(3), pp 1733-1746.
- Huang, Y, Shi, C B, Wan, X X, Li, J L, Zheng, D L and Li, J, 2021. Effect of SiO₂ and B₂O₃ on crystallisation and structure of CaF₂-CaO-Al₂O₃-based slag for electroslag remelting of ultra-supercritical rotor steel, *Journal of Iron and Steel Research International*, 28(12), pp 1530-1540.
- Hwa, L G, Hwang, S L and Liu, L C, 1998. Infrared and Raman spectra of calcium aluminosilicate glasses, *Journal of non-crystalline solids*, 238(3), pp 193-197.
- Ju, J, Gu, Y, Zhang, Q and He, K, 2023. Effect of CaF₂ and CaO/Al₂O₃ ratio on evaporation and melting characteristics of low-fluoride CaF₂-CaO-Al₂O₃-MgO-TiO₂ slag for electroslag remelting, *Ironmaking & Steelmaking*, 50(1), pp 13-20.
- Ju, J, Ji, G, Tang, C, Yang, K. and Zhu, Z, 2021. The effect of Li₂O on the evaporation and structure of low-fluoride slag for vacuum electroslag remelting, *Vacuum*, 183, p 109920.
- Ju, J T, Yang, K S, Gu, Y and He, K, 2022. Effect of Na₂O on Viscosity, Structure and Crystallization of CaF₂-CaO-Al₂O₃-MgO-TiO₂ Slag in Electroslag Remelting, *Russian Journal of Non-Ferrous Metals*, 63(6), pp 599-609.
- Kim, G H, Kim, C S and Sohn, I L, 2013. Viscous behavior of alumina rich calcium-silicate based mold fluxes and its correlation to the melt structure, *ISIJ international*, 53(1), pp 170-176.
- Kim, T S and Park, J H, 2014. Structure-viscosity relationship of low-silica calcium aluminosilicate melts, *ISIJ International*, 54(9), pp 2031-2038.
- Lao, Y, Gao, Y, Deng, F, Wang, Q and Li, G, 2019. Effects of basicity and CaF₂ on the viscosity of CaF₂-CaO-SiO₂ slag for electroslag remelting process, *Metallurgical Research & Technology*, 116(6), p 638.
- Li, J, Shu, Q and Chou, K, 2014. Structural study of glassy CaO-SiO₂-CaF₂-TiO₂ slags by Raman spectroscopy and MAS-NMR, *ISIJ international*, 54(4), pp 721-727.
- McMillan, P and Piriou, B, 1983. Raman spectroscopy of calcium aluminate glasses and crystals, *Journal of Non-Crystalline Solids*, 55(2), pp 221-242.
- Park, H S, Kim, H and Sohn, I, 2011. Influence of CaF₂ and Li₂O on the viscous behavior of calcium silicate melts containing 12 wt pct Na₂O. *Metallurgical and Materials Transactions B*, 42, pp 324-330.
- Park, J H, Min, D J and Song, H.S., 2002. Structural investigation of CaO-Al₂O₃ and CaO-Al₂O₃-CaF₂ slags via Fourier transform infrared spectra, *ISIJ International*, 42(1), pp 38-43.
- Persson, M and Seetharaman, S, 2007. Kinetic studies of fluoride evaporation from slags, *ISIJ International*, 47(12), pp 1711-1717.
- Shi, C B, Li, J, Cho, J W, Jiang, F and Jung, I H, 2015. Effect of SiO₂ on the crystallisation behaviors and in-mold performance of CaF₂-CaO-Al₂O₃ slags for drawing-ingot-type electroslag remelting, *Metallurgical and Materials Transactions B*, 46, pp 2110-2120.
- Shi, C B, Zheng, D L, Shin, S H, Li, J and Cho, J W, 2017. Effect of TiO₂ on the viscosity and structure of low-fluoride slag used for electroslag remelting of Ti-containing steels, *International Journal of Minerals, Metallurgy, and Materials*, 24, pp 18-24.
- Wan, X, Shi, C, Huang, Y, Shu, Q and Zhao, Y, 2023. Effect of SiO₂ and BaO/CaO Mass Ratio on Structure and Viscosity of B₂O₃-Containing CaF₂-CaO-Al₂O₃-Based Slag for Electroslag Remelting of Rotor Steel, *Metallurgical and Materials Transactions B*, 54(1), pp 465-479.
- Wan, X, Shi, C, Zhao, Y and Li, J, 2022. Effect of CaF₂ and Li₂O on structure and viscosity of low-fluoride slag for electroslag remelting of rotor steel, *Journal of Non-Crystalline Solids*, 597, p 121914.
- Wroblewski, K, DiBiaso, B, Fraley, J, Fields, J and Rudoler, S, 2016. Design of ESR Slags According to Requested Physical Properties; Part 2: Density and Viscosity, In *Proceedings of the 2013 International Symposium on Liquid Metal Processing & Casting*, pp 43-46.
- Wroblewski, K, Fraley, J, Fields, J, Werner, R and Rudoler, S, 2011. Design of ESR Slags According to Requested Physical Properties; Part 1: Electrical Conductivity. In *Proceedings of the 2011 International Symposium on Liquid Metal Processing and Casting, Nancy, France*, pp 121-126.
- Xu, R H, Guo, J, Zhang, M C and Guo, H J, 2022. Effect of SiO₂ and TiO₂ on the Crystal Morphology of CaF₂-Al₂O₃-CaO-Based Electroslag Remelting Slag, *Steel research international*, 93(3), p 2100191.
- Yan, X, Pan, W, Wang, X, Zhang, X, He, S and Wang, Q, 2021. Electrical conductivity, viscosity and structure of CaO-Al₂O₃-based mold slags for continuous casting of high-Al steels, *Metallurgical and Materials Transactions B*, 52(4), pp 2526-2535.
- Yeager, J, and Ramanujachary, K, 2007. Method of Measuring Fluoride in Fluxes Using the Fluoride Ion-Selective Electrode." U.S. Patent Application 11/456,815.
- Zheng, D, Li, J and Shi, C, 2020. Development of low-fluoride slag for electroslag remelting: role of Li₂O on the crystallisation and evaporation of the slag, *ISIJ International*, 60(5), pp 840-847.

Zheng, D, Shi, C, Li, J and Ju, J, 2020. Crystallisation kinetics and structure of CaF₂-CaO-Al₂O₃-MgO-TiO₂ slag for electroslag remelting, *ISIJ International*, 60(3), pp 492-498.